Rectangular domain curl polynomial set for optical vector data processing and analysis

Maham Aftab
Logan R. Graves
James H. Burge
Greg A. Smith
Chang-Jin Oh
Dae Wook Kim

SPIE.

Rectangular domain curl polynomial set for optical vector data processing and analysis

Maham Aftab,[a] **Logan R. Graves,**[a] **James H. Burge,**[a] **Greg A. Smith,**[a] **Chang-Jin Oh,**[a] **and Dae Wook Kim**[a,b,*]
[a]The University of Arizona, Large Optics Fabrication and Testing Group, James C. Wyant College of Optical Sciences, Tucson, Arizona, United States
[b]The University of Arizona, Steward Observatory, Tucson, Arizona, United States

Abstract. Rectangular pupils are employed in many optical applications such as lasers and anamorphic optics, as well as for detection and metrology systems such as some Shack–Hartmann wavefront sensors and deflectometry systems. For optical fabrication, testing, and analysis in the rectangular domain, it is important to have a well-defined set of polynomials that are orthonormal over a rectangular pupil. Since we often measure the gradient of a wavefront or surface, it is necessary to have a polynomial set that is orthogonal over a rectangular pupil in the vector domain as well. We derive curl (called **C**) polynomials based on two-dimensional (2-D) versions of Chebyshev polynomials of the first kind. Previous work derived a set of polynomials (called **G** polynomials) that are obtained from the gradients of the 2-D Chebyshev polynomials. We show how the two sets together can be used as a complete representation of any vector data in the rectangular domain. The curl polynomials themselves or the complete set of **G** and **C** polynomials has many interesting applications. Two of those applications shown are systematic error analysis and correction in deflectometry systems and mapping imaging distortion. © *2019 Society of Photo-Optical Instrumentation Engineers (SPIE)* [DOI: 10.1117/1.OE.58.9.095105]

Keywords: measurement and metrology; surface measurements; numerical approximation and analysis; optical instrumentation; information processing; testing.

Paper 190553 received Apr. 22, 2019; accepted for publication Aug. 21, 2019; published online Sep. 24, 2019.

1 Introduction

Previous works highlight the importance of fitting vector slope data in the domain of measurement as well as using orthonormal polynomials for the fitting.[1–3] To summarize, the fit to a nonorthogonal basis set can require many more terms than are necessary, and expansion coefficients themselves are not meaningful, because the value for any particular coefficient changes as the number of expansion terms changes. Also, when fitting to real data, the noise propagation is increased with the use of nonorthogonal basis functions. It is generally simpler and more convenient to use orthogonal polynomials, as they can easily be calculated using the inner product.

In Ref. 3, Chebyshev polynomials are chosen for the basis set from which we will derive the gradient and curl polynomials. This reference also defines gradient polynomials, denoted as the **G** set, which are generated from the gradients of the Chebyshev polynomials of the first kind and are orthogonal over a rectangle. As described in Refs. 3–6, these polynomials can be used for reconstructing high-resolution and free-form surfaces or fitting data from a Shack–Hartmann sensor etc.

In this paper, we will define an additional set of vector polynomials, defined locally as a rotation or a curl, that only consist of terms with zero divergence. We explore the use of these curl polynomials and describe how we can combine them with the gradient polynomials to get a complete set of orthogonal vector polynomials.

Consideration of the curl calculation is used in many areas of optics ranging from vortex beams[7,8] and lithography photomasks[9] to gravitational lensing.[10] In each of these cases, electromagnetic fields with nonzero curl components are used to create or detect significant effects. In other cases, expectation of zero curl in a vector field can improve signal estimation in the presence of noise.[11]

The paper starts with background knowledge in Sec. 2, such as the gradient polynomials and an introduction to the two major applications covered in this work—deflectometry and imaging distortion. Section 3 is dedicated to details of the curl (**C**) polynomials, including their derivation and other details. Section 4 talks about the practical applications and uses of the **G** and **C** polynomials, and concluding remarks are presented in Sec. 5.

2 Background

2.1 Chebyshev Polynomial and Gradient Polynomial Basis

As described in Ref. 3, one can use two-dimensional (2-D) Chebyshev polynomials of the first kind, as well as their derivatives to easily generate orthogonal polynomial sets.

The polynomial basis function is defined as

$$F_n^m(x, y) = T_m(x)T_n(y), \quad (1)$$

where the one-dimensional (1-D) Chebyshev polynomials are

$$T_{m+1}(x) = 2xT_m(x) - T_{m-1}(x),$$
$$T_0(x) = 1, \quad T_1(x) = x. \quad (2)$$

The 2-D set is defined in both x and y on the interval -1 to $+1$, i.e., $-1 \leq x \leq 1$ and the same for y.[12]

Another way to describe the Chebyshev polynomials is using their definitions in terms of sines and cosines. This definition, shown in Eq. (3), is useful if we want to prove the orthogonality of the polynomials and to determine their normalization factor.[3]

$$T_m(x) = \cos[m \cos^{-1}(x)]. \tag{3}$$

The details of these polynomial, their orthonormality, and plots can be found in Ref. 3.

The derivatives of the 1-D Chebyshev polynomials are as follows:

$$T'_m(x) = \frac{m[T_{m-1}(x) - xT_m(x)]}{(1 - x^2)},$$
$$T'_n(y) = \frac{n[T_{n-1}(y) - yT_n(y)]}{(1 - y^2)}. \tag{4}$$

The gradient polynomial set is defined as

$$\vec{G}_j(x, y) = \vec{G}_n^m = \nabla F_n^m(x, y)$$
$$= \frac{\partial}{\partial x} F_n^m(x, y)\hat{i} + \frac{\partial}{\partial y} F_n^m(x, y)\hat{j}. \tag{5}$$

In terms of the 1-D Chebyshev polynomials and their derivatives, the gradient polynomials can be written as

$$\vec{G}_n^m(x, y) = T_n(y)T'_m(x)\hat{i} + T_m(x)T'_n(y)\hat{j}, \tag{6}$$

where the conversion between the single index (j) and the double indices (n, m) can be found in Ref. 3. The notation T' refers to the derivative of the T polynomial [as described in Eq. (4)].

In terms of the recursive Chebyshev polynomials, the gradient polynomials can be written as

$$\vec{G}_n^m(x, y) = \frac{m}{2y(1 - x^2)} [T_{n+1}(y) - T_{n-1}(y)]$$
$$\times [T_{m-1}(x) - xT_m(x)]\hat{i}$$
$$+ \frac{n}{2x(1 - y^2)} [T_{m+1}(x) - T_{m-1}(x)]$$
$$\times [T_{n-1}(y) - yT_n(y)]\hat{j}. \tag{7}$$

The orthogonality and normalization factors are given as

$$\int_{-1}^{1} \int_{-1}^{1} [\vec{G}_j(x, y) \cdot \vec{G}_{j'}(x, y)] \sqrt{1 - x^2} \sqrt{1 - y^2} dx \, dy$$
$$= \begin{cases} 0, & j \neq j' \\ N_G, & j = j' \end{cases}, \tag{8}$$

$$\frac{1}{N_G} \int_{-1}^{1} \int_{-1}^{1} [T_n(y)T'_m(x)\hat{i} + T_m(x)T'_n(y)\hat{j}]$$
$$\cdot [T_{n'}(y)T''_{m'}(x)\hat{i} + T_{m''}(x)T'_{n'}(y)\hat{j}] \sqrt{1 - x^2} \sqrt{1 - y^2} dx \, dy$$
$$= \delta_{mm'} \delta_{nn'}, \tag{9}$$

where m, m', n, and n' are integers and N_G is the normalization factor, which is given by

$$N_G \begin{cases} \frac{\pi^2 n^2}{4}, & m = 0 \\ \frac{\pi^2 m^2}{4}, & n = 0 \\ \frac{\pi^2}{8}(m^2 + n^2), & \text{otherwise} \end{cases}. \tag{10}$$

2.2 Deflectometry

Section 4 describes experimental verifications of the calculations using a method known as deflectometry. This section provides a brief overview of that process.

Deflectometry is a non-null optical metrology method that measures the local slopes on a test surface. The method has been used extensively for precision metrology of symmetric and free-form optical surfaces.[13–17] Because it is a non-null test method, it is a desirable metrology tool for free-form and nonaxisymmetric optics, as well as for metrology during a fabrication process. In both cases, a single deflectometry configuration can maintain testing of the unit under test (UUT) without extensive changes. The measurable surface area of the test optic and slope range, known as the dynamic range, directly depend on the hardware configuration. A deflectometry system utilizes an illuminating source that emits light, sending some rays to the test optic, which are then reflected and recorded by a camera. If a clear line of sight can be made from a camera pixel to the test optic, then the deflectometry system will be able to measure the local slope distribution of the test optic.

In a deflectometry test, the positions of all components in the system must be measured to high accuracy. For testing a concave optic, the camera and source will typically be placed close to the center of curvature (CC) of the optic to achieve closer to a conjugate imaging condition to minimize the required source area. The camera is focused on the test optic surface, such that the camera pixels are mapped to the test optic surface, with each pixel representing a "mirror pixel," or a finite local area over which the local slope will be measured. The source is then precisely modulated such that, for every camera pixel, the precise location on the source that satisfied peak illumination is known.

In visible deflectometry (∼400 to 700 nm), a common source is a digital screen, which can display a phase-stepped sinusoidal pattern in the horizontal and vertical directions. This method, known as phase-stepping deflectometry, has been explored extensively.[18,19] Another option, which has been used for infrared (IR) deflectometry in the ∼7 to 12 μm range as well as the visible range, is a scanning line source, which is scanned in the horizontal and vertical directions.[20,21] In either case, by precisely knowing the start location of a ray at the source, the local point of incidence on the test optic surface, and the final detection point at the camera, the local slope of the test optic can easily be calculated using the law of reflection. The standard setup for a deflectometry test of a concave test optic is shown in Fig. 1.

After measuring the local slopes of the test optic using a deflectometry test, further processing is required to reconstruct the optical surface shape. Typically, this includes further processing to reduce systematic errors and an integration of the local slopes to generate a final reconstructed surface. The integration method can be a zonal[22] or modal[3] approach. It is important to note that any uncertainty in the location of all objects in a deflectometry test will reduce the slope estimation accuracy.
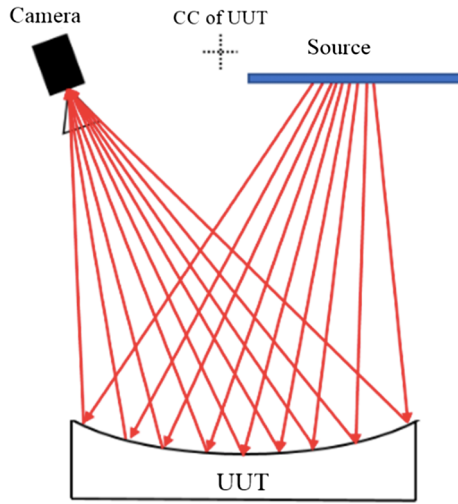
Fig. 1 A deflectometry test utilizes a source, which emits rays that strike a UUT and are reflected, after which some are detected by a camera. For a concave test optic, the source and camera are placed near the CC of the test optic. Then, by precisely measuring the location of all components, the local slopes of the test optic can be output by a deflectometry measurement.

2.3 Imaging Distortion

Imaging distortion[23] is a very common problem in optics. It is a deviation from rectilinear projection. As a consequence of distortion, the image magnification does not remain constant. It either increases or decreases with distance from the optical axis. Although most imaging systems suffer from some amount of distortion, one case where it is very significant is interferometric null testing of steep aspheric surfaces.[24,25] In most cases of imaging distortion, it is relatively easy to quantify and find a mapping correction for the distortion. The most common approach is to place a set of fiducial markers on the optic being tested, which have known, measured locations. The measured image will contain the distorted positions of the fiducials. By constructing a mapping model between the real and the measured fiducial locations, distortion can be calibrated out of the system. One of the ways to construct the mapping distortion model is to use a polynomial fit. Reference 24 gives an example of imaging distortion and introduces a modal fitting method for it, based on the **S** and **T** polynomials,[1,2] which are a complete vector domain set, based on the gradient and curl of Zernike polynomials, respectively, and orthogonalized across a circular aperture. They can be used to represent any vector data in the circular domain. In Sec. 4.2, we provide an example of system distortion for a telescope and propose its fitting with two vector polynomial-based methods—one using the **S** and **T** and another, the **G** and **C** polynomials.

3 Curl Polynomial Set

It is known that vector fields can be uniquely specified by giving their divergence and curl within a region and the normal component over the boundary. This leads to Helmholtz's theorem, which allows us to express the vector field (**V**) as the sum of an irrotational (∅) and a solenoidal part (**P**), as follows:

$$\vec{V} = \nabla\varnothing + \nabla \times \vec{P}. \tag{11}$$

The divergence of the vector field is given as

$$\nabla \cdot \vec{V} = \nabla^2\varnothing. \tag{12}$$

Its curl is given as

$$\nabla \times \vec{V} = \nabla \times (\nabla \times \vec{P}). \tag{13}$$

Since the **G** polynomials are defined as the gradients of scalar functions, they have no curl component.

We want to derive another vector set (**C** polynomials) that have zero divergence. So, **C** polynomial set has zero ∅, but nonzero **P**. Hence it is defined as

$$\vec{C} = \nabla \times \vec{P} = \begin{vmatrix} \hat{i} & \hat{j} & \hat{k} \\ \frac{\partial}{\partial x} & \frac{\partial}{\partial y} & \frac{\partial}{\partial z} \\ P_x & P_y & P_z \end{vmatrix}. \tag{14}$$

Like the **G** polynomials, the **C** polynomials are defined in the x–y plane only. One way to do this is to use a scalar φ, which is a function of x and y, to represent **P** as follows:

$$\vec{P} = \varphi\hat{k}. \tag{15}$$

Then, the curl polynomials are given as

$$\vec{C}_n = \nabla \times \varphi_n\hat{k} = \hat{i}\frac{\partial\varphi_n}{\partial y} - \hat{j}\frac{\partial\varphi_n}{\partial x}. \tag{16}$$

For the **C** polynomials, we can use the same basis functions (F) that were used for generating the **G** polynomials. Then, by Eq. (8), we know that the **C** polynomials will be mutually orthogonal. Hence, we can also define them as

$$\vec{C}_j(x,y) = \vec{C}_n^m(x,y) = \frac{\partial}{\partial y}F_n^m(x,y)\hat{i} - \frac{\partial}{\partial x}F_n^m(x,y)\hat{j},$$

$$\vec{C}_n^m(x,y) = T_m(x)T_n'(y)\hat{i} - T_n(y)T_m'(x)\hat{j}. \tag{17}$$

The conversion between the double indices (n,m) and single index (j) is the same as for **G** polynomials.[3]

Here, $\vec{G}_i(x,y)$ and $\vec{C}_i(x,y)$ are orthogonal to each other at any point in a unity normalized rectangle for terms where the Laplacian is nonzero.

Using Eqs. (2) and (4), we can define the **C** polynomials in terms of the recursive Chebyshev polynomials of the first kind as

$$\begin{aligned} \vec{C}_n^m(x,y) = & \frac{n}{2x(1-y^2)}[T_{m+1}(x) - T_{m-1}(x)] \\ & \times [T_{n-1}(y) - yT_n(y)]\hat{i} \\ & - \frac{m}{2y(1-x^2)}[T_{n+1}(y) - T_{n-1}(y)] \\ & \times [T_{m-1}(x) - xT_m(x)]\hat{j}. \end{aligned} \tag{18}$$

The orthonormality of the basis set is defined the same way as with the gradient set:

$$\int_{-1}^{1}\int_{-1}^{1}[\vec{C}_j(x,y).\vec{C}_{j'}(x,y)]\sqrt{1-x^2}\sqrt{(1-y^2)}\mathrm{d}x\,\mathrm{d}y = \begin{cases} 0, & j \neq j' \\ N_C, & j = j' \end{cases}. \tag{19}$$

This can also be described as

$$\frac{1}{N_C}\int_{-1}^{1}\int_{-1}^{1}\frac{[-T_n(y)T'_m(x)\hat{j} + T_m(x)T'_n(y)\hat{i}].}{[-T_{n'}(y)T'_{m'}(x)\hat{j} + T_{m'}(x)T'_{n'}(y)\hat{i}]}\sqrt{1-x^2}\sqrt{1-y^2}\mathrm{d}x\,\mathrm{d}y = \delta_{mm'}\delta_{nn'}. \tag{20}$$

The normalization factor is the same as for **G** polynomials, as given in Eq. (10).

$$N_C \begin{cases} \frac{\pi^2 n^2}{4}, & m = 0 \\ \frac{\pi^2 m^2}{4}, & n = 0 \\ \frac{\pi^2}{8}(m^2 + n^2), & \text{otherwise} \end{cases}. \tag{21}$$

The derivation of orthonormality and how to get the normalization factor is nearly identical to Ref. 3. Table 1 lists the first 15 curl polynomials and Appendix 1 illustrates several terms graphically.

Table 1 is simplified using the following relations:

$$T_0(x) = 1, \quad T_0(y) = 1, \quad T_1(x) = x, \quad T_1(y) = y,$$
$$T'_0(x) = 0, \quad T'_0(y) = 0, \quad T'_1(x) = 1, \quad T'_1(y) = 1. \tag{22}$$

3.1 Two Sets to Completely Define a Vector Field

Similar to the circular case in reference 2, we can visualize **G** polynomials as irrotational vector fields, which have zero curl everywhere, and **C** polynomials as solenoidal vector fields, which have zero divergence everywhere. These two fields have some overlap where both divergence and curl are zero, which is known as the Laplacian vector field. The overlapped area contains terms derived from the corresponding scalar $\varnothing$ polynomials (in our case, the 2-D Chebyshev polynomials) whose Laplacian is 0. If $\varnothing$ (in our case, F) represents wavefront, these terms correspond to a wavefront with zero net curvature at any point in the pupil.

To completely specify the orthogonal rectangular domain, we can combine the **G** and **C** polynomials, and to ensure that the Laplacian is not counted twice, the **C** polynomial set should be modified to only include the independent terms (i.e., all **C** terms except the ones that are common with the Laplacians). The Laplacian operator is defined as the divergence of the gradient of a function. It can be calculated empirically using the sine- and cosine-based definition of the **G** polynomials,[3] and it can be programmed numerically using the recursive definitions. A simple implementation would be to take the divergence of the **G** polynomials and for the terms that equal zero, remove them from the complete set.

Table 1 Curl polynomials in terms of Chebyshev polynomials of the first kind and associated derivatives.

m	n	$\vec{C}_j$	Simplified form	Expressed as Chebyshev polynomials of first kind
0	0	$\vec{C}_0$	$0\hat{i} - 0\hat{j}$	0
1	0	$\vec{C}_1$	$-\hat{j}$	$\frac{-T_0(y)[T_0(x)-xT_1(x)]}{(1-x^2)}\hat{j}$
0	1	$\vec{C}_2$	$\hat{i}$	$\frac{T_0(x)[T_0(y)-yT_1(y)]}{(1-y^2)}\hat{i}$
2	0	$\vec{C}_3$	$-T'_2(x)\hat{j}$	$-2\frac{T_0(y)[T_1(x)-xT_2(x)]}{(1-x^2)}\hat{j}$
1	1	$\vec{C}_4$	$-y\hat{j} + x\hat{i}$	$\frac{-T_1(y)[T_0(x)-xT_1(x)]}{(1-x^2)}\hat{j} + \frac{T_1(x)[T_0(y)-yT_1(y)]}{(1-y^2)}\hat{i}$
0	2	$\vec{C}_5$	$T'_2(y)\hat{i}$	$2\frac{T_0(x)[T_1(y)-yT_2(y)]}{(1-y^2)}\hat{i}$
3	0	$\vec{C}_6$	$-T'_3(x)\hat{j}$	$-3\frac{T_0(y)[T_2(x)-xT_3(x)]}{(1-x^2)}\hat{j}$
2	1	$\vec{C}_7$	$-yT'_2(x)\hat{j} + T_2(x)\hat{i}$	$-2\frac{T_1(y)[T_1(x)-xT_2(x)]}{(1-x^2)}\hat{j} + \frac{T_2(x)[T_0(y)-yT_1(y)]}{(1-y^2)}\hat{i}$
1	2	$\vec{C}_8$	$-T_2(y)\hat{j} + xT'_2(y)\hat{i}$	$\frac{-T_2(y)[T_0(x)-xT_1(x)]}{(1-x^2)}\hat{j} + 2\frac{T_1(x)[T_1(y)-yT_2(y)]}{(1-y^2)}\hat{i}$
0	3	$\vec{C}_9$	$T'_3(y)\hat{i}$	$3\frac{T_0(x)[T_2(y)-yT_3(y)]}{(1-x^2)}\hat{i}$
4	0	$\vec{C}_{10}$	$-T'_4(x)\hat{j}$	$-4\frac{T_0(y)[T_3(x)-xT_4(x)]}{(1-x^2)}\hat{j}$
3	1	$\vec{C}_{11}$	$-yT'_3(x)\hat{j} + T_3(x)\hat{i}$	$-3\frac{T_1(y)[T_2(x)-xT_3(x)]}{(1-x^2)}\hat{j} + \frac{T_3(x)[T_0(y)-yT_1(y)]}{(1-y^2)}\hat{i}$
2	2	$\vec{C}_{12}$	$-T_2(y)T'_2(x)\hat{j} + T_2(x)T'_2(y)\hat{i}$	$-2\frac{T_2(y)[T_1(x)-xT_2(x)]}{(1-x^2)}\hat{j} + 2\frac{T_2(x)[T_1(y)-yT_2(y)]}{(1-y^2)}\hat{i}$
1	3	$\vec{C}_{13}$	$-T_3(y)\hat{j} + xT'_3(y)\hat{i}$	$\frac{-T_3(y)[T_0(x)-xT_1(x)]}{(1-x^2)}\hat{j} + 3\frac{T_1(x)[T_2(y)-yT_3(y)]}{(1-y^2)}\hat{i}$
0	4	$\vec{C}_{14}$	$T'_4(y)\hat{i}$	$4\frac{T_0(x)[T_3(y)-yT_4(y)]}{(1-y^2)}\hat{i}$

As with the gradient polynomials, each term is a combination of two terms, both containing one Chebyshev polynomial and one Chebyshev polynomial derivative terms each. Appendix 1 gives the quiver plots of the first few nontrivial curl polynomials.

3.2 Data Fitting in the Rectangular Domain

Both **G** and **C** polynomials (like the 2-D Chebyshev polynomials of the first kind, from which they are derived) are orthogonal in the rectangular domain.[3] If data are taken over a nonsquare rectangular domain, the longer normalized dimension will span the full range of −1 to 1, whereas the shorter dimension will be scaled proportional to its relative size to the longer dimension. The actual implementation of this depends on the user. References [3] to [5] contain examples of surface and wavefront reconstructions using the **G** polynomials over nonsquare rectangular domains. It is expected that data fitting over a nonsquare rectangular domain would require more terms than the same data over a square domain of the same total area.

As a demonstration, simulated curl data were generated over a square domain, with 600×600 pixels. A square portion of 200×200 pixels and a rectangular portion of 400×100 pixels were cropped out to represent the same area but different aspect ratio domain cases. Both data sets were fit by the same number of **C** polynomials and fitting residual results were compared in terms of percentage root mean square (RMS) error, which is defined as

$$\text{Percentage RMS error} = [\text{RMS (fitted data}$$
$$- \text{simulated data)}/\text{RMS (simulated data)}] \times 100[\%].$$

$$(23)$$

It is observed that the percentage RMS error is higher for nonsquared data, as compared to squared data case, for the same number of fitted polynomials. For example, when the first 50 **C** polynomials are used, the percentage RMS error for square domain and nonsquare domain data are 0.8% and 1.4%, respectively. Figure [2] shows the downsampled quiver plots (1.5× magnified for ease of viewing) of the square and nonsquare domain simulated data and the reconstructions, using the first 50 **C** polynomials in each case. Also, Table [2] presents the change in percentage RMS error as a function of the fitted **C** polynomial numbers. However, it is worth noting that the specific number of required terms also depends on the frequency content of the given data to fit. The presented result in Fig. [2] and Table [2] is only an example and not a generalized conclusion.

4 Employing the Vector Polynomial Set in Practical Applications

4.1 Deflectometry Data Analysis Using C Polynomials

To demonstrate the vector polynomial's fitting ability for a misaligned optical testing case, a highly free-form Alvarez lens, as shown in Fig. [3], is measured using a phase-shifting deflectometry setup, as described in Sec. [2.2]. The Alvarez
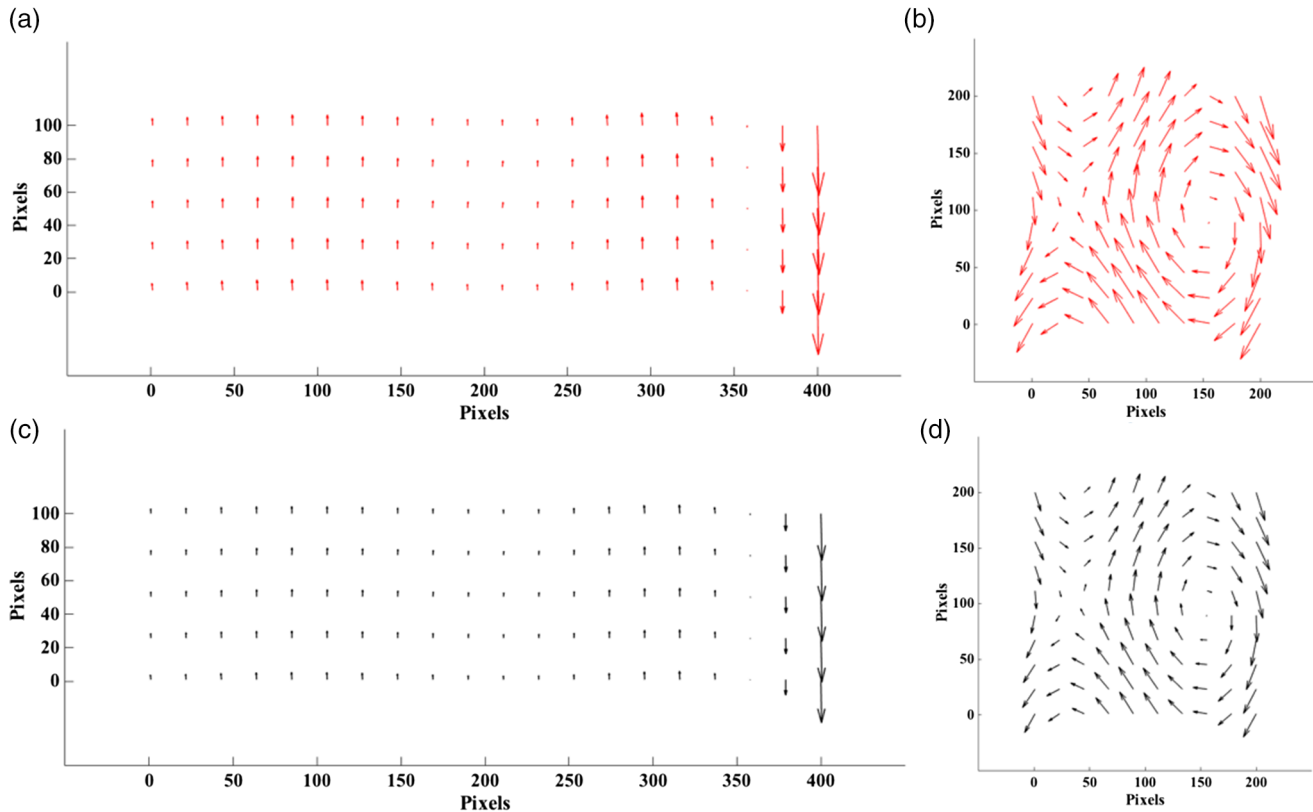

Fig. 2 Downsampled, 1.5× magnified quiver plots from (a) simulated nonsquare domain data, (c) fitted nonsquare domain data (using the first 50 **C** polynomials), (b) simulated square domain data, and (d) fitted square domain data (using the first 50 **C** polynomials).

Table 2 Percentage RMS error comparison for nonsquare and square domain cases, as a function of the number of **C** polynomials used in the fitting.

No. of **C** polynomials	Percentage RMS error (%)	
	Nonsquare domain	Square domain
10	60.0	24.0
15	35.5	3.0
25	2.9	1.4
50	1.4	0.8

lens, made from a 1-in.-diameter substrate, was created using a diamond-turned computer-numeric control process. The process was set to generate a 6-mm central aperture inside of the disk, having 17 μm of horizontal coma and −17 μm of 45-deg trefoil, described as Zernike polynomials. A liquid crystal display was utilized as the source and was mounted in place above the Alvarez lens. A camera manufactured by Point Grey was additionally mounted in place above the Alvarez lens. The Alvarez lens was placed on a precision manual rotation stage, with rotation accuracy of ±0.05 deg. The clear aperture of the Alvarez lens for this measurement setup was a square of length 5.6 mm, thus modeling the case of a rectangular domain, as a rectangular aperture free-form optic was not readily available for testing. This being said, it must be noted that free-form rectangular optics are becoming increasingly common, with cases such as augmented reality lenses and telescopes utilizing such optics.[26] The goal of this example is to demonstrate the data-processing capability using real data from an optical component in the rectangular domain.

To test the optic, a deflectometry measurement was taken at a 0-deg clocking position for the Alvarez lens. Next, the Alvarez lens was rotated and measurements were taken at every 0.5 deg clocking of the lens.

The goal is to be able to successfully check for nonorthogonality error of the deflectometry setup and be able to determine the amount of error (i.e., degree of misclocking) so it can be corrected/accounted for.

First, we construct a "clocking error" model based on known clocking errors from the setup. We first measure the gradients when the Alvarez lens is set to 0 deg. Then, we start to rotate the optic by known amounts and collect the slope maps for all the rotations. Next, we only use the x-gradient map from the rotated sets, and all the y-gradients are the unrotated y-gradient, i.e., the y slope at 0 deg. This simulates the situation when the system is set up in such a way that the x and y slopes are not taken at a 90-deg angle but have some misclocking between them. A practical example of this could be the nonorthogonality between the position of the scanning hot wire (line source) in the two scanning directions (x and y) for the case of IR deflectometry.[20]

In this example, we are simulating a situation where the system is set up such that there is nonorthogonality between the x and y slope measurements. Since this nonorthogonality is a system-based error alone and is not associated with the scalar Alvarez lens surface itself, we use only **C** polynomials to model the impact on the acquired slope data. The ideal slope data from a scalar surface (e.g., Alvarez lens surface) should have zero curl components; thus, the **C** polynomial fit to an acquired data set affected by the measurement uncertainty in the scanning axis can be used as a direct indicator to diagnose, sense, and calibrate the measurement axis uncertainty.

For this experiment, measurements were made every 0.5 deg from 0 deg to 2.5 deg. These data sets were fitted with the first 50 **C** polynomials. The following equation sets were used for fitting (which is very similar to data fitting for **G** polynomials).

If the curl of the lens surface is represented by $\nabla \times W$, then a_k is the expansion coefficient of the **C** polynomial set (whose terms are represented by C_k) and N is the number of coefficients used in the fitting, which, in this example, is 50.

$$\nabla \times W(x, y) = \sum_{k=1}^{N} a_k \vec{C}_k. \qquad (24)$$

Since we are dealing with discrete data, we can write Eq. (24) as

$$R = \vec{C}a, \qquad (25)$$

where R is a column vector of P data values, a is a column vector containing the N expansion coefficients, and C is a $P \times N$ matrix representing the values of the **C** polynomials at the locations of the data points.

The coefficients can then be found using a pseudoinverse
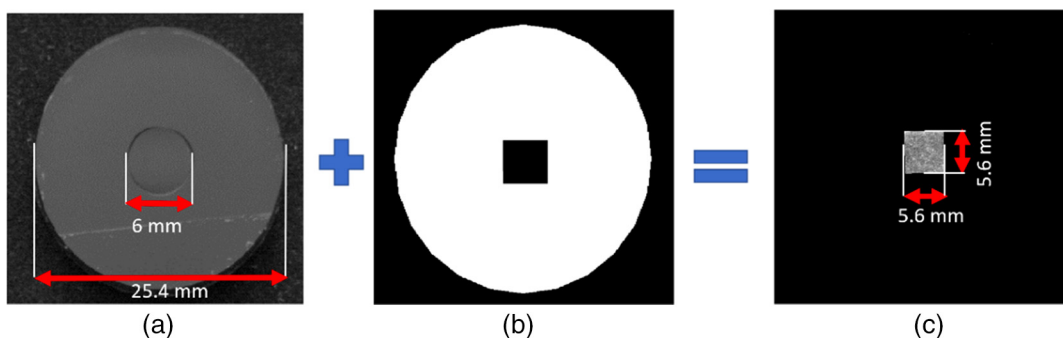
$$a = (\vec{C}^T \vec{C})^{-1} \vec{C}^T R. \qquad (26)$$

(a)   (b)   (c)

Fig. 3 (a) The Alvarez lens (b) with a clear aperture of 5.6 × 5.6 mm² was designed to have only horizontal coma and 45-deg trefoil. Phase-shifting deflectometry was used to measure (c) the clear aperture lens area at various clocking positions.
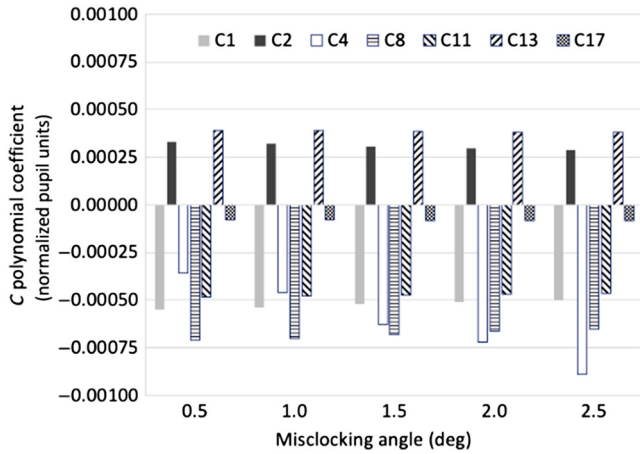
Fig. 4 Histogram of **C** polynomial coefficients (e.g., "C13" is the 13th **C** polynomial term value C_{13}) used in the analytical Alvarez lens model, as a function of misclocking angles.

Based on the polynomial terms, which stood out from all the processed measurements and showed a steady change (increase or decrease) as the misclocking between the two slopes increased, we constructed a model that predicted the slope clocking mismatch between the x and y slopes when an "unknown" misclocking was introduced.

The **C** polynomials used in the analysis were 1, 2, 4, 8, 11, 13, and 17. Figure 4 shows the change in polynomial values, as misclocking is increased. The absolute value of the polynomials at each misclocking angle is not important. What matters is their relative values. These results were input to a least-squares fit model, where a linear combination of each of these polynomial terms was used to calculate an overall transformation matrix. When an unknown deflectometry measurement is taken, it can be decomposed into the first 50 (or fewer) **C** polynomial terms. Values for **C** polynomials are used to calculate the coefficients of the transformation matrix, which is the predicted clocking for the input measurement. The following equation can be used to visualize this fit mathematically:

$$R = a_1C_1 + a_2C_2 + a_4C_4 + a_8C_8 + a_{11}C_{11} + a_{13}C_{13} + a_{17}C_{17},$$
(27)

where R is the rotation angle vector of the unknown clocking error, a_k are the expansion coefficients of the **C** polynomials [as described in Eq. (24)], and C_k are the specific **C** polynomials we have considered in this model.

To test the model, we used two measurements—one at 0.6 deg and the other at 2.3 deg. Table 3 shows the error between the predicted and the actual misclocking. Both predictions showed good agreement with the actual values. Figure 5 shows the value of select **C** polynomials for the data used for constructing the model, as well as the two trial clocked data sets (0.6 deg and 2.3 deg).

4.2 Imaging Distortion Modeling Using **G** and **C** Polynomials

For this case study, as shown in Fig. 6(a), we use a retrace-able distortion map, as shown in Fig. 6(b), from a standard Zemax library model of a three-mirror anastigmat (TMA)

Table 3 **C** polynomial-based misclocking estimation performance for Alvarez lens deflectometry data analysis case

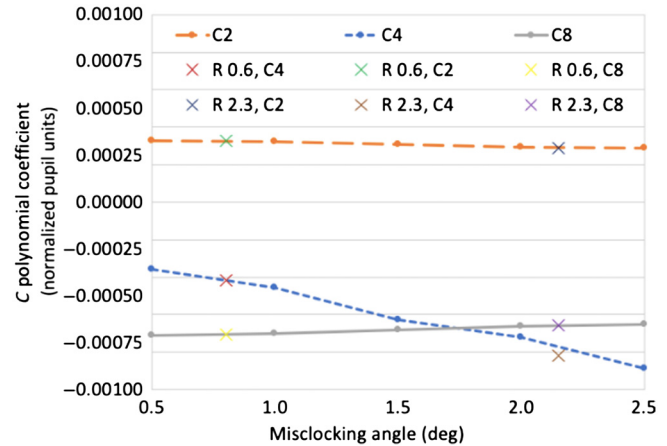| True (T) (deg)	Computed (C) (deg)	Error (T − C) (deg)	% Error (%)
0.6	0.6024	−0.0024	−0.4000
2.3	2.3917	−0.0917	−3.9870

Fig. 5 Selected **C** polynomial terms (C2, C4, and C8) used in Alvarez lens deflectometry misclocking modeling, shown as plots with lines. Overlaid are corresponding **C** polynomial values from trial data sets (0.6 deg and 2.3 deg), shown as large cross-shaped markers. This is written in the legend as (for example): "R 0.6, C4" meaning the C_4 polynomial coefficient for the trial data at 0.6 deg.

with rectangular aperture. The TMA camera system parameters are listed in Table 4, and its optical layout is shown in Fig. 6(a).

The distortion map is fit in two ways and compared: one using the **G** and **C** polynomials and the other using Zernike-based **S** and **T** polynomials.[1,2] Since Zernike polynomials, as well as both **S** and **T** basis sets, are orthogonal over a unit circle, and in this example we have rectangular data, the use of Zernike-based polynomial set is not ideal to represent/model the distortion vector distribution. This is not a problem for the **G** and **C** polynomial sets because of their orthogonality in the rectangular domain. For simple distortion, which is simulated without noise, the corner points are not likely to have a significant impact on fitting performance. However, in practical systems with noise, the removal of points for Zernike-based fitting can lead to inaccurate results.

For both polynomial sets, the first 12 (6 gradient and 6 curl) polynomials were chosen. It was ensured that the common terms in both sets (i.e., for which the Laplacian are zero) were only counted once. Reference 2 lists the first 12 nontrivial **T** polynomials, as well as the Laplacian = 0 terms for those 12 terms, so these were selected. For the Zernike-based fit, we used terms 2 to 7 of the **S** polynomials and terms 4, 7, 8, and 11 to 13 of the **T** polynomial set. Terms 1–6 of the **C** polynomials and terms 3 and 5–9 of the **G** polynomials were used for the Chebyshev-based fit.

The RMS error, and percent RMS error, in x and y positions, defines the residual error (from both fits). It is calculated as
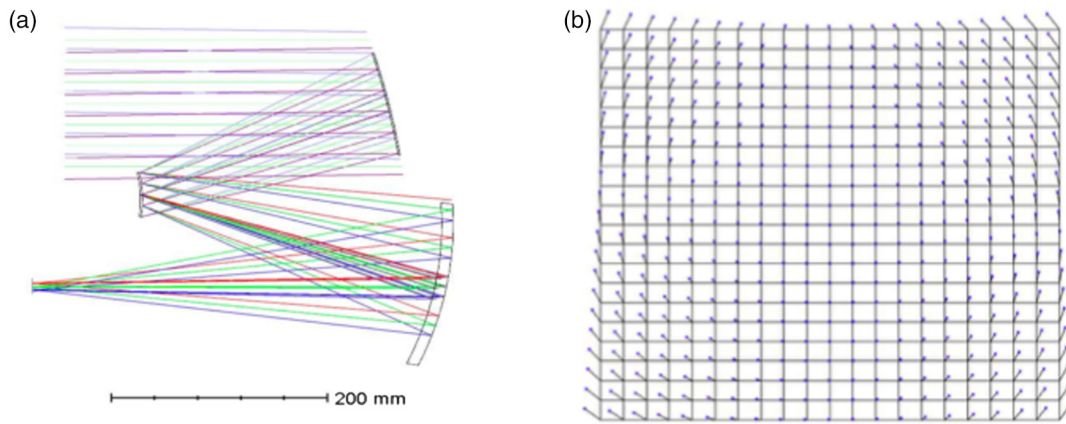
(a)

├─────────────┤ 200 mm

(b)

Fig. 6 (a) Schematic representation of the simulated TMA camera system in the Zemax library.[26] (b) Distortion map for this system using 20×20 grid sampling with $15\times$ arrow size magnification.

Table 4 Parameters of the simulated TMA camera system retraceable by accessing the standard Zemax library model.[27]

Parameters	Values
Effective focal length (in air at system temperature and pressure)	216.22 mm
Back focal length	−383.78 mm
Image space F/#	1.53
Working F/#	1.56
Stop radius	35.36 mm
Maximum radial field	1.41 deg
Primary wavelength	1.00 μm

%Error

$$= 100\% \times [\mathrm{RMS\,(real\ error)/RMS\,(reference\ position)}],$$
$$(28)$$

where reference position is the ideal (simulated) distortion, i.e., predicted real position from the distortion map.

As can be seen from the results in Fig. 7 and Table 5, the **G** and **C** fitting provides more accurate representation of the ideal distortion map, with lower errors in both x and y positions.

A current literature search did not show an easy way to find the overlapping (Laplacian = 0) terms for the **S** and **T** polynomials beyond the 12 terms used in this example. To keep consistency in the comparison, only 12 terms for the **G** and **C** polynomials were also used, although we can easily use many more terms and easily obtain the overlap terms (through numerical programming, for example), thus reducing the error even further than shown in Table 5. Part of this ease is due to the fact that the **G** and **C** polynomials are obtained from direct derivatives of the scalar function (F), whereas the **S** and **T** polynomials require additional manipulation of their scalar (Zernike) basis set. Table 6 shows the improvement in distortion correction as more terms of the **G** and **C** polynomials are used, as well as the time taken for the
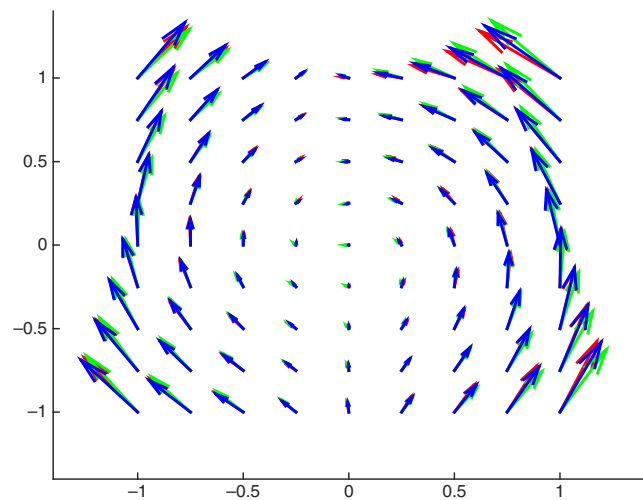

Fig. 7 (a) Quiver plots from the TMA camera's distortion fitting. Red arrows are the ideal (i.e., simulated values), green arrows are results from **S** and **T** fitting, and blue arrows are the results from **G** and **C** fitting. The quiver plot is downsampled and arrows are magnified 1.5×. The x and y axes are normalized image plane coordinates [the domain from Fig. 6(b) is normalized from −1 to +1].

Table 5 Fitting performance comparison of the two vector polynomial set cases to represent/model the TMA camera's distortion map.

	S and **T** polynomial fitting		**G** and **C** polynomial fitting	
	x position	y position	x position	y position
Real error (μm)	0.593	0.654	0.255	0.285
% Error (%)	12.44	8.30	5.35	3.62

fitting (including polynomial generation). Note that the number of terms in this table refers to the total number of **G** and **C** polynomial terms, i.e., 20 terms would mean 10 **G** and 10 **C** polynomial terms. The error reduction begins to saturate around 50 terms (25 **G** and 25 **C** terms), as we are possibly reaching the limit of numerical accuracy.

As a comparison, the Zernike-based (**S** and **T** polynomial) fitting took about 0.11 s when the first 12 polynomials were

Table 6 Residual error and processing time comparison as a function of the total number of **G** and **C** polynomials used to represent/model the TMA camera's distortion map.

No. of terms	% Error (%)		Time (s)
	x position	y position	
12	5.35	3.62	0.02
20	0.82	3.12	0.03
50	0.09	0.05	0.08

used (results from Table 5). We would like to acknowledge that the processing time depends on the specific numerical implementation of the fitting method and may improve with better algorithms. Although our implementation of either the **G** and **C** or the **S** and **T** polynomial sets was not targeted for optimum processing time, this example serves as a baseline comparison for the two fitting methods.

5 Concluding Remarks

We have extended the previously defined set of vector polynomials that are the gradients of a scalar function and included an orthonormal set that has zero divergence everywhere and can be considered the rotation or curl. The scalar function to generate the curl is the 2-D Chebyshev polynomial of the first kind.

The combined set of gradient and curl polynomials (considering only the independent terms, i.e., where the common terms having Laplacian = 0 are only counted once) is useful for fitting any continuously differentiable vector functions in the rectangular domain. In particular, it is useful in modeling or fitting mapping distortions. Numerical examples prove that the combined set works well to define a measured vector field and can be used to easily calibrate out the misalignment state of a deflectometry test configuration.

The orthogonality in the chosen domain is critical because it allows specific **G** and **C** polynomial terms to be associated with physical parameters of the system. If a nonorthogonal basis set was chosen, the polynomial terms would lose their meaning and so the system/systematic error analysis, as presented in Sec. 4, would not be possible. Second, both **G** and **C** polynomial sets are simple and efficient to generate. Although conceptually **G** and **C** polynomial generation is similar to **S** and **T** (Zernike-based) polynomials, the details of obtaining the gradient and curl sets from the scalar basis set is different. While **S** and **T** polynomials require the gradient and curl of Zernike polynomials to be orthogonalized across a circular aperture (using the Gram–Schmidt orthogonalization), the **G** and **C** polynomials can be obtained more directly from the scalar Chebyshev basis set. One implication of this could be the feasibility to generate many high order terms, with accuracy and numerical efficiency. This has many practical implications, such as representing mid-to-high spatial frequencies,[3,4] fitting free-form surfaces,[3,6] or analyzing vector data from surfaces with missing data (such as optics with fiducials or scratches).

6 Appendix A

To visualize the **C** polynomials, quiver plots (made in MATLAB) are provided for a few of the low-order, nontrivial polynomials (Fig. 8). These plots represent the vector **C** polynomials as arrows, with one axis on each figure representing the x axis and the other representing the y axis.
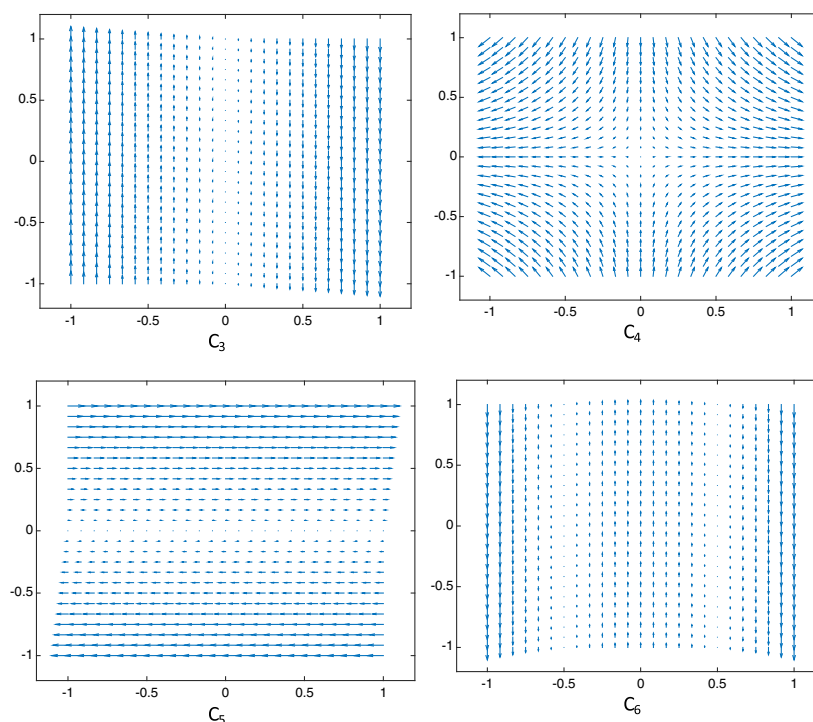

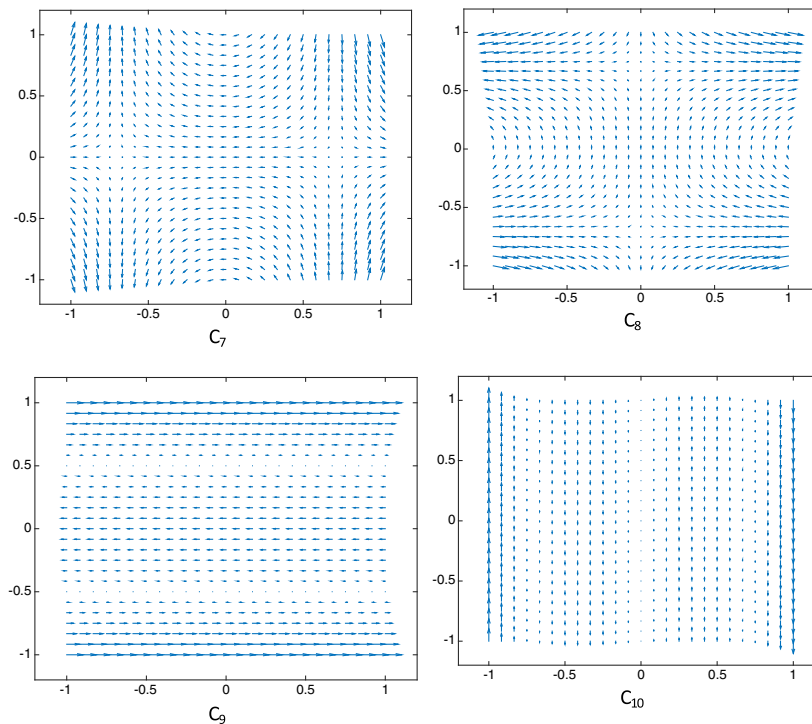**Fig. 8** Quiver plots of a few nontrivial **C** polynomials.

Fig. 8 (*Continued.*)

References

1. C. Zhao and J. H. Burge, "Orthonormal vector polynomials in a unit circle, part I: basis set derived from gradients of Zernike polynomials," *Opt. Express* **15**(26), 18014–18024 (2007).
2. C. Zhao and J. H. Burge, "Orthonormal vector polynomials in a unit circle, part II: completing the basis set," *Opt. Express* **16**(9), 6586–6591 (2008).
3. M. Aftab et al., "Modal data processing for high resolution deflectometry," *Int. J. Precis. Eng. Manuf.-Green Technol.* **6**, 255–270 (2019).
4. M. Aftab et al., "Chebyshev gradient polynomials for high resolution surface and wavefront reconstruction," *Proc. SPIE* **10742**, 1074211 (2018).
5. M. Aftab et al., "Adaptive Shack–Hartmann wavefront sensor accommodating large wavefront variations," *Opt. Express* **26**(26), 34428–34441 (2018).
6. I. Trumper, M. Aftab, and D. W. Kim, "Freeform surface selection based on parametric fitness function using modal wavefront fitting," *Opt. Express* **27**(5), 6815–6831 (2019).
7. X.-L. Wang et al., "Optical orbital angular momentum from the curl of polarization," *Phys. Rev. Lett.* **105**, 253602 (2010).
8. C. H. Schmitz et al., "Tuning the orbital angular momentum in optical vortex beams," *Opt. Express* **14**(15), 6604–6612 (2006).
9. A. Shanker et al., "Transport of intensity phase imaging in the presence of curl effects induced by strongly absorbing photomasks," *Appl. Opt.* **53**, J1–J6 (2014).
10. P. A. R. Ade et al., "Bicep2/Keck array VIII: measurement of gravitational lensing from large-scale B-mode polarization," *Astrophys. J.* **833**, 228 (2016).
11. X. Jing et al., "Shape reconstruction based on zero-curl gradient field estimation in a fringe reflection technique," *Appl. Opt.* **57**, 4135–4144 (2018).
12. F. Liu et al., "Analyzing optics test data on rectangular apertures using 2-D Chebyshev polynomials," *Opt. Eng.* **50**(4), 043609 (2001).
13. D. W. Kim et al., "Optical metrology systems spanning the full spatial frequency spectrum," in *Front. Opt.*, Optical Society of America, p. FW5G.4 (2016).
14. R. Huang et al., "High-accuracy aspheric x-ray mirror metrology using Software Configurable Optical Test System/deflectometry," *Opt. Eng.* **54**(8), 084103 (2015).
15. J. Burke et al., "Qualifying parabolic mirrors with deflectometry," *J. Eur. Opt. Soc.—Rapid publ.* **8**, 1–6 (2013).
16. C. J. Oh et al., "Fabrication and testing of 4.2m off-axis aspheric primary mirror of Daniel K. Inouye Solar Telescope," *Proc. SPIE* **9912**, 99120O (2016).
17. L. R. Graves et al., "Model-free deflectometry for freeform optics measurement using an iterative reconstruction technique," *Opt. Lett.* **43**, 2110–2113 (2018).
18. A. E. Lowman et al., "Measurement of large on-axis and off-axis mirrors using Software Configurable Optical Test System (SCOTS)," *Proc. SPIE* **10706**, 107061E (2018).
19. R. Huang, "High precision optical surface metrology using deflectometry," PhD Thesis, The University of Arizona (2015).
20. T. Su et al., "Measuring rough optical surfaces using scanning long-wave optical test system. 1. Principle and implementation," *Appl. Opt.* **52**, 7117–7126 (2013).
21. T. Su et al., "Scanning long-wave optical test system: a new ground optical surface slope test system," *Proc. SPIE* **8126**, 81260E (2011).
22. W. H. Southwell, "Wave-front estimation from wave-front slope measurements," *J. Opt. Soc. Am.* **70**, 998–1006 (1980).
23. G. Hollows and N. James, Distortion | Edmund Optics. Edmund Optics Worldwide, https://www.edmundoptics.com/resources/application-notes/imaging/distortion/ (accessed 3 March 2019).
24. C. Zhao and J. H. Burge, "Orthonormal vector polynomials in a unit circle, application: fitting mapping distortions in a null test," *Proc. SPIE* **7426**, 74260V (2009).
25. M. Novak, C. Zhao, and J. H. Burge, "Distortion mapping correction in aspheric null testing," *Proc. SPIE* **7063**, 706313 (2008).
26. H. Hua, X. Hu, and C. Gao, "A high-resolution optical see-through head-mounted display with eyetracking capability," *Opt. Express* **21**(25), 30993–30998 (2013).
27. Zemax Opticstudio, Zemax LLC (2018).

Maham Aftab is a senior design engineer at ASML, USA. She received her BS degree in engineering sciences from GIK Institute, Pakistan; MS degree in applied physics from TU Delft, The Netherlands; MS degree in optics, matter, and plasma from École Polytechnique, France; and MS and PhD degrees in optical sciences from the University of Arizona. Her current research interests include hardware and software design and analysis and mathematical study and development for optical metrology systems, particularly for high-resolution and free-form optics.

Dae Wook Kim is an assistant professor of optical sciences and astronomy at the University of Arizona. His research area covers precision optical engineering, including interferometry and deflectometry. He is the chair of the Optical Manufacturing and Testing (SPIE) and Optical Fabrication and Testing (OSA) conferences. He is a senior member of OSA and SPIE and has served as an associate editor for *Optics Express*.

Biographies of the other authors are not available.